A Computational Framework for Evaluating Dynamic Motion Performance of Diversified eVTOLs using Fluid-Rigid Body Coupled Simulation with Route Tracking

Ayato Takii[1][0000−0003−3257−7640], Hiroto Sato[2], Masashi Yamakawa[2], Makoto Tsubokura[1], Takahiro Ikeda[2], Yusei Kobayashi[2], Shinichi Asao[3], Seiichi Takeuchi[3], and

[1] Kobe University, 1-1, Rokkodai-cho, Nada-ku, Kobe, 657-8501, Hyogo, Japan
[2] Kyoto Institute of Technology, Matsugasaki, Sakyo-ku, 606-8585, Kyoto, Japan
[3] College of Industrial Technology, 1-27-1, Amagasaki, Hyogo 661-0047, Japan

Abstract. As electric vertical take-off and landing (eVTOL) aircraft diversify in configuration, quantitative comparison of dynamic motion performance at the conceptual design stage has become a critical challenge. This study proposes a computational framework that integrates route-tracking control into a fluid–rigid body coupled simulation based on the Moving Computational Domain (MCD) method and multi-axis sliding mesh technique. A PID controller combined with a look-ahead point algorithm enables autonomous simulation of a common four-phase flight route (ascent, forward acceleration, deceleration, and descent). The framework is applied to two eVTOL configurations: a compact coaxial Octorotor (400 kg) and a large Dodecarotor (1400 kg). Four motion performance metrics—maneuverability, responsiveness, energy efficiency, and ride comfort—are quantitatively evaluated. Fluid–rigid body coupling captures unsteady aerodynamic effects overlooked by conventional rigid-body models: the Octorotor experiences 24% greater aerodynamic drag during forward acceleration, and its fluid-coupled energy consumption (1.87 kWh) is 60% higher than estimates based solely on rotor RPM. Furthermore, while the Dodecarotor offers 1.4× better per-passenger energy efficiency due to its larger rotor disk area, its ride comfort is significantly compromised (RMS acceleration: 3.75 vs. 0.238 m/s^2), identifying a fundamental trade-off between efficiency and comfort. This framework provides high-fidelity quantitative guidance for vehicle concept selection and control optimization in model-based eVTOL development.

Keywords: Computational Fluid Dynamics · eVTOL · Route Tracking · Fluid-Rigid Body Coupling · Energy Efficiency.

1 Introduction

Electric vertical take-off and landing (eVTOL) aircraft have emerged as a next-generation aerial transportation mode with broad applications, including urban

ICCS Camera Ready Version 2026
To cite this paper please use the final published version:
DOI: 10.1007/978-3-032-29921-5_22

traffic alleviation, medical and disaster response, and regional transit infrastructure [11, 3]. In eVTOL development, Model-Based Development (MBD)—where simulation-driven decision-making occurs in the upstream design phases—is becoming increasingly critical [19]: early quantitative evaluation of flight characteristics, safety, and energy efficiency simultaneously reduces development costs and ensures product quality. Since physical flight tests require substantial investment of both time and capital [6], expectations for high-fidelity Computational Fluid Dynamics (CFD) simulations continue to grow.

Numerical simulations for eVTOLs have traditionally evolved in isolated domains, such as the aerodynamic analysis of isolated propellers [7], CFD of the full aircraft in steady states [21], or flight control simulations utilizing rigid-body dynamics models [16]. However, these approaches fall short when analyzing unsteady phenomena during complex, continuous flight maneuvers, such as acceleration, deceleration, and turning. In realistic flight scenarios, the relative head- or tailwinds induced by the aircraft's own motion exert highly nonlinear effects on rotor thrust and power consumption. Furthermore, aerodynamic interference and response delays associated with changes in the angle of attack during acceleration cannot be captured by simple equation-of-motion-based control models. Previous research [8] has demonstrated that the presence or absence of fluid coupling leads to significant discrepancies in predicting flight dynamics during disturbance evaluations; a parallel challenge exists in evaluating general motion performance. To establish a common baseline for comparing diverse aircraft configurations (e.g., varying rotor counts, layouts, and sizes), simulations conducted under identical route-tracking conditions are essential. Nevertheless, most existing studies remain confined to steady-state or speed-control-based evaluations, leaving a unified framework capable of quantitatively comparing different models unavailable. Although our recent study [10] assessed the safety of these two eVTOL models during rotor failure, it did not address the evaluation of dynamic motion performance during continuous route-tracking flight. The present study addresses this gap.

The objective of this study is to establish a computational framework that integrates route-tracking control into fluid-rigid body coupled simulations, thereby proposing a methodology for the quantitative evaluation and comparison of the dynamic motion performance of diverse eVTOLs. The primary novelties of this framework are threefold: First, it integrates a route-tracking algorithm based on PID control and a look-ahead point strategy into a fluid solver powered by the Moving Computational Domain (MCD) method and multi-axis sliding mesh techniques. Second, it defines four specific evaluation metrics—maneuverability, responsiveness, efficiency, and smoothness—establishing a systematic approach to extracting data directly applicable to MBD. Third, through basic maneuver simulations (acceleration and deceleration) at fixed angles of attack, it quantifies the differences in aerodynamic interference characteristics between the two aircraft, demonstrating that fluid-rigid body coupling captures unsteady aerodynamic phenomena unattainable by rigid-body models alone. The remainder of this paper is organized as follows: Section 2 details the numerical methods

ICCS Camera Ready Version 2026
To cite this paper please use the final published version:
DOI: 10.1007/978-3-032-29921-5_22

for fluid-rigid body coupling and the implementation of route-tracking control. Section 3 defines the motion performance evaluation metrics. Section 4 outlines the computational setup. Section 5 presents the results and discussion of the basic maneuver performance and the route-tracking simulations, followed by the conclusions in Section 6.

2 Numerical Approach and Computational Framework

2.1 Governing Equations for Fluid

Given the necessity of conducting long-duration, unsteady flight simulations of eVTOLs, computational efficiency is paramount. Thus, the compressible Euler equations are adopted as the governing equations for the fluid domain. The governing equations in conservative vector form are expressed as:

$$\frac{\partial \boldsymbol{Q}}{\partial t} + \nabla \cdot \boldsymbol{F}(\boldsymbol{Q}) = \boldsymbol{0} \tag{1}$$

where $\boldsymbol{Q} = (\rho, \rho u, \rho v, \rho w, e)^{\mathsf{T}}$ is the vector of conserved variables, and $\boldsymbol{F}$ denotes the convective flux. Here, u, v, and w are the velocity components in the x, y, and z directions, respectively, and e represents the total energy per unit volume. The numerical flux is evaluated using the approximate Riemann solver based on Roe's method [9], incorporating Harten's entropy fix ($\varepsilon = 0.2$) [4]. High-order spatial accuracy is achieved via the MUSCL approach coupled with a van Leer-type limiter [5]. Time integration is performed using the Crank–Nicolson method for time discretization and the rational Runge–Kutta method [15].

2.2 Fluid-Rigid Body Coupling via the MCD Method

When an eVTOL traverses a substantial spatial domain, discretizing the entire flight path with a computational grid is prohibitively expensive. To navigate this, this study employs the Moving Computational Domain (MCD) method [17, 20], which confines a finite-sized computational grid strictly to the immediate vicinity of the aircraft and translates this grid in tandem with the vehicle's motion. This approach enables the simulation of arbitrary flight maneuvers while preserving high grid quality. This moving mesh concept is concurrently applied to the rotors to handle their rotational motion. Furthermore, to accommodate multi-rotor eVTOLs where multiple rotors possess independent rotational axes, the multi-axis sliding mesh technique is incorporated [14].

The aircraft's motion is governed by a 6-degree-of-freedom Newton-Euler rigid-body dynamics model [13]. The fluid solver and the rigid-body motion solver are integrated via a weak coupling scheme. Specifically, at each time step, the fluid solver first updates the flow field subjected to grid velocity boundary conditions and integrates the pressure over the aircraft surface to evaluate the aerodynamic loads. Subsequently, the rigid-body motion solver explicitly integrates the Newton-Euler equations to update the aircraft's position and attitude, which are then fed back into the MCD method for the subsequent step.

ICCS Camera Ready Version 2026
To cite this paper please use the final published version:
DOI: 10.1007/978-3-032-29921-5_22

2.3 Rotor Control Model and Route Tracking

Mixing Algorithm. To generate the necessary control forces and moments, optimal rotational speeds must be dictated to each rotor. This is achieved effectively by allocating the four control inputs required in the aircraft coordinate system (throttle, elevator, roll, and yaw) to individual rotors via a mixing algorithm. For overactuated systems with more than four rotors, a unique increment in rotational speeds for all rotors is computed using a mixing matrix based on the pseudo-inverse: $M = \bar{M}^{\mathsf{T}}\left(\bar{M}\bar{M}^{\mathsf{T}}\right)^{-1}$. Here, $\bar{M}$ is a matrix determined purely by the aircraft geometry and rotor layout. The rotor thrust T and torque Q required to formulate $\bar{M}$ are modeled as proportional to the square of the rotational speed ω, i.e., $T = A\omega^2$ and $Q = B\omega^2$. The coefficients A and B were derived prior through independent fluid simulations of the isolated rotors.

PID Controller. An outer-loop PID controller based on altitude and horizontal positional errors generates a target acceleration. Subsequently, an inner-loop PID controller, which inversely calculates a target attitude angle from this acceleration, stabilizes the aircraft's orientation. The control gains are initially determined using the Ziegler–Nichols method and refined within a standalone control/kinematics model (control model) stripped of fluid effects. After confirming the absence of overshoot across all parameters within this control model, the gains are applied to the full fluid-structure coupled flight behavior simulation. Final minor adjustments to the gains are made based on the outcomes of the fully coupled fluid computations.

3 Evaluation Metrics for Motion Performance

To evaluate the dynamic motion performance of eVTOLs in a manner directly applicable to MBD, this study defines the following four metrics. These metrics are calculated from time-series data extracted from the fluid-rigid body coupled simulations, facilitating a rigorous quantitative comparison among different aircraft concepts.

Maneuverability Maneuverability is assessed by the linearity of the acceleration in the direction of travel, $a_{\parallel}$, with respect to the angle of attack.
To quantify this linearity against the angle of attack α—defined as the arctangent of the ratio of the y-velocity to the x-velocity in the aircraft coordinate system—the time history of an indicator h, defined by the following equation, is analyzed:

$$h = \frac{a_{\parallel}}{\sin\alpha} \tag{2}$$

If h remains constant throughout a given flight phase, it indicates that acceleration responds linearly to the angle of attack, representing high maneuverability. Coupling with the fluid simulation enables the direct observation of non-linearities (i.e., fluctuations in h) induced by increased aerodynamic drag or multi-rotor aerodynamic interference.

ICCS Camera Ready Version 2026
To cite this paper please use the final published version:
DOI: 10.1007/978-3-032-29921-5_22

Responsiveness Responsiveness quantifies the transmission delay from a control input to the vehicle's actual physical motion. A cross-correlation method is applied to the target signal $\boldsymbol{s}_d$ and the actual output signal $\boldsymbol{s}$ over an evaluation window T_{win} starting at time t_0, the onset of a transient maneuver where targets shift. Defining k_1 and k_2 as the start and end steps of the evaluation interval, the function of n:

$$R(n) = \sum_{k=k_1}^{k_2} \boldsymbol{s}(k)\, \boldsymbol{s}_d(k-n) \tag{3}$$

is computed, and the sample shift n_d maximizing $R(n)$ within $0 < n < k_2 - k_1$ is identified. The equivalent time delay is then $T_d = n_d\, \Delta t$. A dimensionless time delay $\eta = T_d / T_{\text{win}}$ is also introduced to enable comparisons independent of the evaluation window length. Furthermore, to evaluate responsiveness in the frequency domain, Bode plots of the forward velocity v_x relative to the forward external force F_x are generated, allowing an assessment of the gain and phase delay to low-frequency inputs across different aircraft.

Efficiency Efficiency is a metric evaluating the energy consumption essential for executing a flight mission. The instantaneous power consumption of all rotors is given by:

$$P = \sum_i \frac{\omega_i\, \tau_i}{k} \tag{4}$$

where ω_i and τ_i are the rotational speed and the aerodynamic load torque of the i-th rotor, respectively. The coefficient $k = 0.72$ accounts for the combined efficiency of the motor and Electronic Speed Controller (ESC), estimated as the product of 90% aerodynamic load efficiency and 80% motor/ESC efficiency [18, 2]. The total consumed energy E over the flight is obtained via numerical integration using the trapezoidal rule.

Smoothness Smoothness acts as a proxy for passenger ride comfort and is evaluated via the frequency-weighted Root Mean Square (RMS) acceleration, a_v, in accordance with the ISO 2631-1 standard. The frequency-weighted RMS accelerations $a_{\omega x,\text{rms}}$, $a_{\omega y,\text{rms}}$, and $a_{\omega z,\text{rms}}$ are computed by applying the ISO 2631-1 Wd filter (to the x and z axes) or the Wk filter (to the y axis). These are aggregated using the following equation:

$$a_v = \sqrt{(k_x\, a_{\omega x,\text{rms}})^2 + (k_y\, a_{\omega y,\text{rms}})^2 + (k_z\, a_{\omega z,\text{rms}})^2} \tag{5}$$

In this study, the axial weighting factors are assigned as $k_x = k_z = 1.4$ and $k_y = 1.0$. Based on the magnitude of a_v, ride comfort is classified into six defined categories: "Comfortable" ($< 0.315\,\text{m/s}^2$), "A little uncomfortable" (0.315–0.63), "Fairly uncomfortable" (0.5–1.0), "Uncomfortable" (0.8–1.6), "Very uncomfortable" (1.25–2.5), and "Extremely uncomfortable" (> 2.0).

ICCS Camera Ready Version 2026
To cite this paper please use the final published version:
DOI: 10.1007/978-3-032-29921-5_22

4 Simulation Setup

4.1 Target Aircraft

Two morphologically distinct multi-rotor eVTOL configurations are analyzed in this study (Fig. 1).

Octorotor eVTOL: This model is a compact, lightweight aircraft equipped with four pairs of coaxial counter-rotating rotors (eight rotors in total). Its overall dimensions are $4 \times 4 \times 2\,\mathrm{m}$, with a gross weight of 400 kg and a seating capacity of one passenger. The moments of inertia are $(I_x, I_y, I_z) = (51, 326, 319)\,\mathrm{kg\,m^2}$. The rotor diameter is 1.3 m, and the nominal rotational speed during hover is 1930 RPM. This model has been utilized in previous aerodynamic analyses [1, 12] and functions as the baseline aircraft for validating the proposed framework.

Dodecarotor eVTOL: This model represents a large aircraft featuring 12 rotors mounted on arm structures arranged in a spatially expansive, dome-like configuration. Its overall dimensions span $13 \times 13 \times 3\,\mathrm{m}$, with a weight of 1400 kg (3.5 times that of the Octorotor) and a seating capacity for three passengers. The moments of inertia are $(I_x, I_y, I_z) = (4560, 7580, 4570)\,\mathrm{kg\,m^2}$. The rotor diameter is 2.4 m, hovering at approximately 1400 RPM.

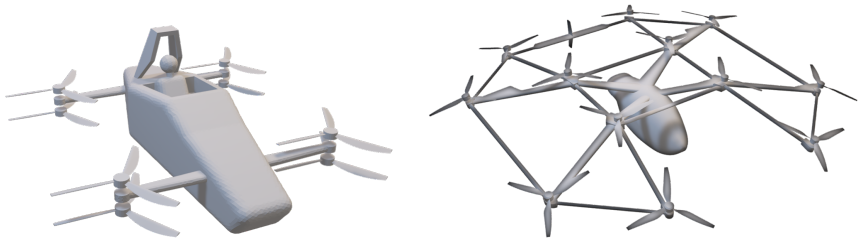

(a) Octorotor eVTOL (b) Dodecarotor eVTOL

Fig. 1: Target aircraft models.

Computational grids for both aircraft are composed of unstructured tetrahedral cells. Fine cells are clustered near the aircraft surfaces to capture the intricate rotor geometries accurately, gradually coarsening toward the outer boundaries of the computational domain. The minimum grid spacing is approximately 6 mm on the rotor surfaces. The total grid count for the Octorotor is around 3.0 million cells (comprising ∼2.0 million cells in the main body domain and ∼12,000 cells per rotor domain), while the Dodecarotor utilizes about 5.8 million cells (∼2.0 million cells in the body domain and ∼31,000 cells per rotor).

4.2 Flight Route and Simulation Conditions

To ensure an equitable comparison of performance between different scaling classes, a common target flight route is established (Fig. 2). This reference route

ICCS Camera Ready Version 2026
To cite this paper please use the final published version:
DOI: 10.1007/978-3-032-29921-5_22

consists of four sequential waypoints, corresponding to an ascent of 5 m, a forward progression of 50 m, and a subsequent descent of 5 m. Simulations are executed independently for both the Octorotor and the Dodecarotor, allowing for a quantitative comparison of their dynamic motion performance over identical trajectories.

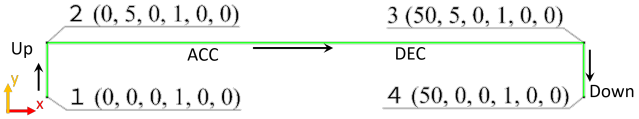

Fig. 2: Common target flight route used for both aircraft. The route consists of four phases: ascent, forward acceleration, deceleration, and descent.

To navigate this continuous flight path, a route-tracking algorithm incorporating a look-ahead point logic is implemented [22]. As the aircraft approaches a target waypoint, the algorithm automatically transitions to the subsequent waypoint once the distance between the vehicle's center of gravity and the current target falls below a threshold of 0.3 m. During the forward acceleration phase, the aircraft purposefully pitches down, converting a component of vertical thrust into forward acceleration; conversely, during the deceleration phase, it pitches up to initiate braking. This entire sequence of dynamic maneuvers is realized autonomously within the coupled simulation environment.

5 Results and Discussion

5.1 Basic Maneuver Performance Comparison

Prior to engaging the route-tracking control, basic maneuver simulations executed under fixed angle-of-attack conditions establish the baseline aerodynamic differences between the Octorotor and Dodecarotor. These preliminary tests emphasize the necessity of full fluid-rigid body coupling.

Hovering Performance. The surrounding flow fields of both models during hover are illustrated in Fig. 3. The Octorotor's coaxial design produces a concentrated downwash approximately 37% wider than an isolated rotor configuration, while the Dodecarotor's dome-like arrangement induces inward-merging flows with strong interaction between the inner rotors and structural arms. The thrust coefficient ratio $A_{\mathrm{Dod}}/A_{\mathrm{Oct}} = 4.05$ confirms significantly higher per-rotor thrust efficiency attributable to the Dodecarotor's larger rotor diameter.

Acceleration Performance. Flow fields captured during forward acceleration, with the pitch angle statically constrained at $-15°$, are presented in Fig. 4. Maximum sustained accelerations were 1.85 m/s^2 for the Octorotor and 2.45 m/s^2 for

ICCS Camera Ready Version 2026
To cite this paper please use the final published version:
DOI: 10.1007/978-3-032-29921-5_22

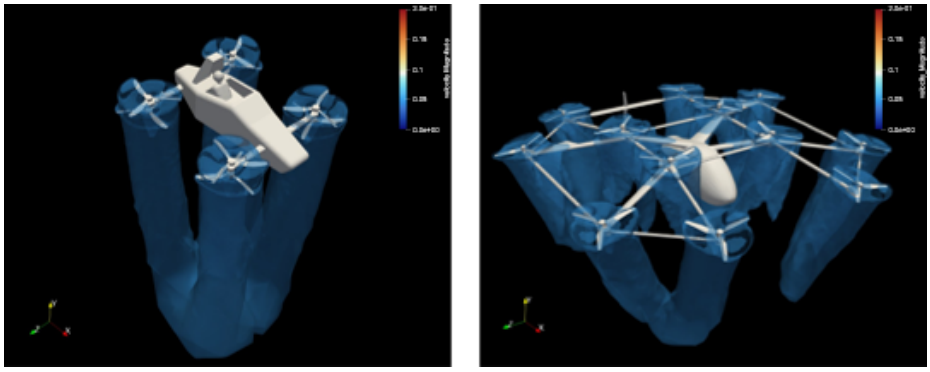

Fig. 3: Comparison of velocity isosurfaces (15 m/s) during hovering. Left: Octorotor eVTOL (concentrated downwash from co-axial counter-rotating rotors). Right: Dodecarotor eVTOL (flows merging toward the center from the dome-arranged rotors).

the Dodecarotor. The Octorotor experiences approximately 24% greater aerodynamic drag, attributable to its relatively large frontal area despite the compact coaxial arrangement. In the later stages of acceleration, the response becomes non-linear due to escalating parasitic drag—a transient aerodynamic effect invisible to rigid-body kinematics alone. Furthermore, the dynamic mapping between pitch angle and resultant forward acceleration obtained in this phase directly informs the velocity scheduling utilized in the route-tracking control logic.

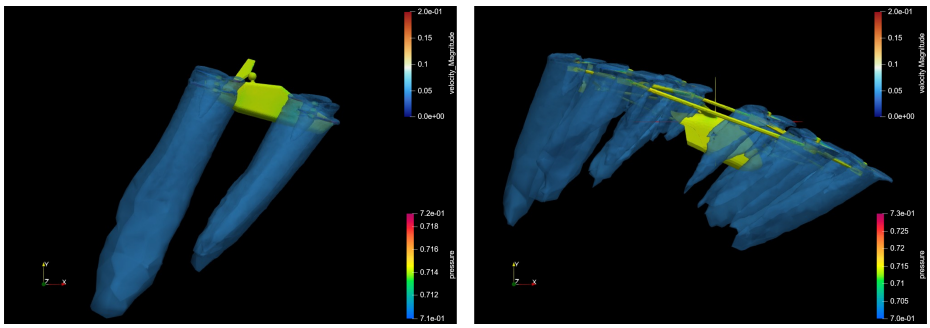

Fig. 4: Flow fields during forward acceleration (pitch angle = −15°, velocity isosurfaces at 15 m/s). Octorotor (left) exhibits 24 % higher aerodynamic drag than Dodecarotor (right).

Deceleration Performance. Braking performance metrics derived from an emergency stopping maneuver, executing with the pitch angle rigidly set to +30°

ICCS Camera Ready Version 2026
To cite this paper please use the final published version:
DOI: 10.1007/978-3-032-29921-5_22

Table 1: Comparison of brake performance.

	Octorotor	Dodecarotor
Max. deceleration [m/s^2]	6.11	5.93
Braking distance [m]	27.5	26.9
Braking time [s]	5.57	6.49

from an initial cruise speed of 50 km/h, are summarized in Table 1. The analysis juxtaposes peak deceleration rates, required braking distances, and total maneuver times. While the maximum achieved deceleration values appear closely matched—6.11 m/s^2 for the Octorotor versus 5.93 m/s^2 for the Dodecarotor—the temporal dynamics diverge significantly. Specifically, the Dodecarotor requires nearly a full additional second to attain complete cessation of motion, underscoring a slower dissipative convergence following the initial braking transient.

These results confirm that the Octorotor's compact geometry renders it more susceptible to drag penalties, and that such unsteady aerodynamic effects require full fluid–body coupling to capture accurately. Figure 5 visualizes the flow during braking (pitch +30°): the Octorotor shows a large high-pressure region ahead and a broad recirculation zone beneath the fuselage, while the Dodecarotor's low-velocity envelope is more compact and shifted aft.

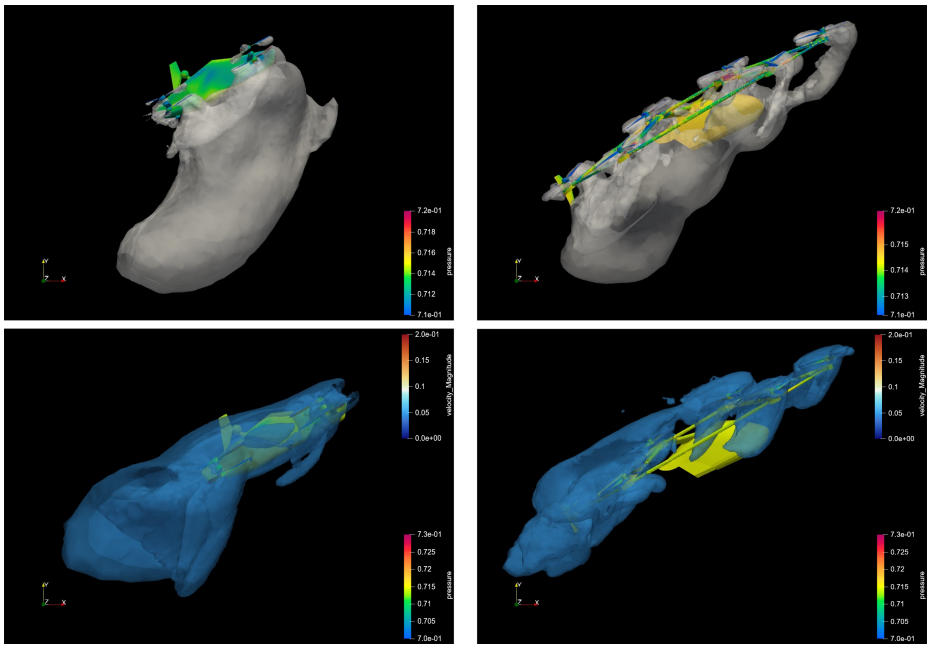

Fig. 5: Comparison of deceleration flow fields (pitch angle +30°). Left: Octorotor, Right: Dodecarotor. Top: pressure isosurface, Bottom: velocity isosurface.

ICCS Camera Ready Version 2026
To cite this paper please use the final published version:
DOI: 10.1007/978-3-032-29921-5_22

Table 2: Differences in energy consumption due to calculation method variations (Octorotor eVTOL). E_1, E_2, E_3: energy in each phase; E: total energy.

Method	E_1 [kWh]	E_2 [kWh]	E_3 [kWh]	E [kWh]
RPM only	0.148	0.922	0.104	1.17
Aerodynamic load torque	0.117	1.513	0.243	1.87
Estimate with inertia torque	0.136	1.498	0.266	1.90

5.2 Route Tracking Simulation: Octorotor eVTOL

Route Tracking Performance. The Octorotor demonstrated high-fidelity adherence to the target trajectory persistently across all four designated flight phases, finalizing the complete maneuver in precisely 21.0 seconds. The duration of purely forward translation (Phase 2) measured 16.8 seconds. While this represents a protracted execution compared to the 9.3 seconds reported under a simplified open-loop forward velocity constraint in historical data [12], this discrepancy natively reflects the purposefully conservative tuning of the control gains deployed here to strictly suppress aggressive velocity overshoot scenarios. Positional deviations computed normal to the intended route vectors remained trivially negligible throughout the entire flight regime, providing robust validation for the underlying tracking logic.

Maneuverability and Aerodynamic Nonlinearity. During Phase 2, the maneuverability metric h (Eq. (2)) remained nearly constant (peak $h_{\max} \approx 2.54\,\mathrm{m/s^2}$), confirming a proportional relationship between pitch angle and forward acceleration. Toward the end of the acceleration phase, h decreased due to rising aerodynamic drag, consistent with the non-linear behavior observed in the basic maneuver tests (Section 5.1).

Responsiveness. Cross-correlation analysis revealed a clear hierarchy of latencies: the x-position loop registered $T_d = 3.00\,\mathrm{s}$ ($\eta = 1.00$), while rotor RPM responded nearly instantaneously at $T_d = 2.92\,\mathrm{ms}$ ($\eta = 9.72 \times 10^{-4}$). The fluid-dynamic thrust delay ($T_z \approx 11\,\mathrm{ms}$) was an order of magnitude faster than the control system bandwidth, confirming that fluid inertia in thrust response can be treated as negligible in control design.

The Bode plot (Fig. 6) shows a flat gain at low frequencies and $-20\,\mathrm{dB/decade}$ roll-off at higher frequencies, with phase approaching $-90°$, characteristic of a stable first-order system.

Efficiency. Table 2 compares energy estimates from three methods. The RPM-only estimate ($E = 1.17\,\mathrm{kWh}$) underestimates the aerodynamic-torque-based result ($E = 1.87\,\mathrm{kWh}$) by over 60%, as fluctuating inflow conditions during Phase 2 substantially increase rotor load torque. Including mechanical inertial torque ($E = 1.90\,\mathrm{kWh}$) adds only a marginal correction, confirming that aerodynamic loading dominates over inertial effects.

ICCS Camera Ready Version 2026
To cite this paper please use the final published version:
DOI: 10.1007/978-3-032-29921-5_22

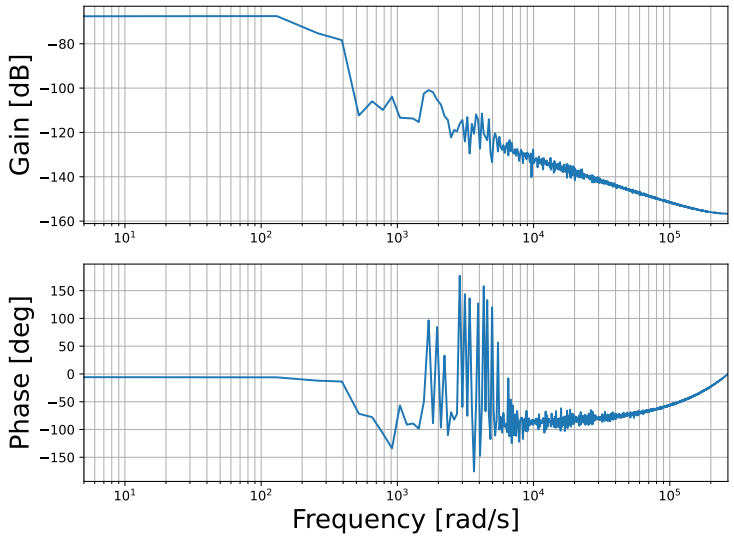

Fig. 6: Bode diagram of forward velocity v_x versus forward force F_x during the initial forward motion of the Octorotor eVTOL.

Table 3: Evaluation of ride smoothness for Octorotor eVTOL.

Phase	Status	$a_{\omega x}$	$a_{\omega y}$	$a_{\omega z}$	a_v	Evaluation
1	Ascending	0.285	0.204	0.00707	0.449	A little uncomfortable
2	Parallel movement	0.143	0.0313	0.0145	0.203	Comfortable
3	Descending	0.0172	0.114	0.00287	0.116	Comfortable
1–3	Overall	0.159	0.081	0.0132	0.238	Comfortable

Smoothness. The comprehensive ISO 2631-1 compliant ride-comfort metrics characterizing the Octorotor are provided in Table 3. The overall ride comfort index is $a_v = 0.238\,\mathrm{m/s^2}$ ("Comfortable"). The worst phase is ascent ($a_v = 0.449\,\mathrm{m/s^2}$, "A little uncomfortable"), where vertical thrust variation dominates. Both the forward flight and descent phases fall within the "Comfortable" range.

5.3 Route Tracking Simulation: Dodecarotor eVTOL

Route Tracking and Maneuverability. Figure 7 compares the trajectories and dynamic states of both vehicles. Despite large differences in mass and geometry, both tracked the route with comparable fidelity. However, the maneuverability metric h diverged significantly: the Dodecarotor exhibited strong non-linearity in the latter half of the acceleration phase, driven by localized inflow gradients across its widely distributed rotor disks, where forward-facing rotors suffered lift penalties while inner rotors encountered wake entrainment.

ICCS Camera Ready Version 2026
To cite this paper please use the final published version:
DOI: 10.1007/978-3-032-29921-5_22

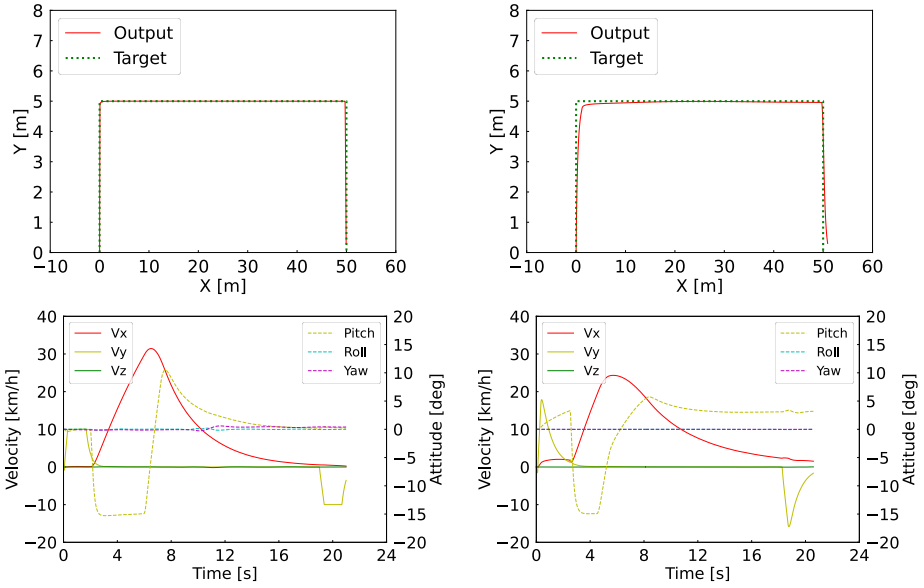

Fig. 7: Comparison of flight behavior between Octorotor eVTOL (left) and Dodecarotor eVTOL (right). Top: flight trajectories. Middle: velocity and attitude time histories. Bottom: lateral and attitude error.

Responsiveness. The Bode plot of the Dodecarotor (Fig. 8) shows similar low-frequency gain behavior to the Octorotor, but the phase asymptote shifts from $-90°$ to approximately $-70°$. This difference indicates that the Dodecarotor's greater mass expands the frequency range over which inertial resistance dominates aerodynamic drag, altering the effective dynamic response.

Efficiency. The Dodecarotor consumed approximately 2.1 times more total energy than the Octorotor. However, accounting for its $3.5\times$ greater weight and $3\times$ passenger capacity, the per-passenger efficiency is approximately 1.4 times better. This advantage is consistent with actuator disk theory: the Dodecarotor's thrust coefficient ratio of 4.05 reflects reduced disk loading and improved hovering efficiency.

Smoothness. The Dodecarotor's ride comfort is substantially worse, as shown in Table 4. The overall index is $a_v = 3.75\,\mathrm{m/s^2}$ ("Extremely uncomfortable"), approximately 16 times higher than the Octorotor. Vertical acceleration during ascent and descent exceeded $10\,\mathrm{m/s^2}$, dominated by the $a_{\omega y}$ axis, revealing that standard altitude-rate PID controllers lack jerk-rate limiting adequate for heavy-payload configurations. This result identifies a fundamental trade-off: the high thrust levels required for large eVTOLs are inherently incompatible with acceptable ride comfort under standard PID control.

ICCS Camera Ready Version 2026
To cite this paper please use the final published version:
DOI: 10.1007/978-3-032-29921-5_22

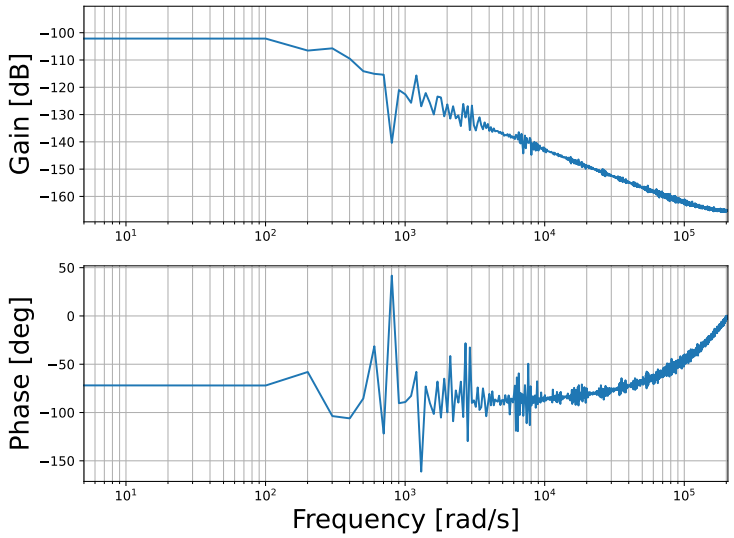

Fig. 8: Bode diagram of forward velocity v_x versus forward force F_x during the initial forward motion of the Dodecarotor eVTOL. The phase is approximately $-70°$, compared to $-90°$ for the Octorotor.

Table 4: Evaluation of ride smoothness for Dodecarotor eVTOL.

Phase	Status	$a_{\omega x}$	$a_{\omega y}$	$a_{\omega z}$	a_v	Evaluation
1	Ascending	0.304	11.43	0.00966	11.44	Extremely uncomfortable
2	Parallel movement	0.248	0.847	0.00323	0.916	Fairly uncomfortable
3	Descending	0.125	3.408	0.0213	3.412	Extremely uncomfortable
1–3	Overall	0.245	3.735	0.0077	3.75	Extremely uncomfortable

Synthesizing these findings defines targeted use domains: the compact Octorotor excels in environments demanding agility, rapid command responsiveness, and passenger comfort, making it well-suited for short urban hop scenarios. In contrast, the Dodecarotor's large disk-area advantages confer superior per-passenger efficiency, directing its viability toward steady-state, long-haul transport applications. This framework has demonstrated the capability to deliver rigorous, quantitatively actionable engineering insights directly from the earliest phases of conceptual design.

6 Conclusion

This study developed a computational framework integrating autonomous route-tracking with high-fidelity fluid–rigid body coupled simulation to evaluate the dynamic performance of diverse eVTOL architectures. By employing the Moving Computational Domain (MCD) method and a PID-based navigation algorithm,

ICCS Camera Ready Version 2026
To cite this paper please use the final published version:
DOI: 10.1007/978-3-032-29921-5_22

the framework successfully simulated a standardized four-phase flight trajectory. Comparative analysis of the Octorotor and Dodecarotor models yielded four key findings. First, the aerodynamically bluff Octorotor experienced 24% higher drag during forward acceleration compared to the Dodecarotor. Conversely, the larger Dodecarotor experienced a nearly one-second stopping delay during braking, confirming that capturing unsteady loads requires full fluid–body coupling. Second, the robust control loops maintained negligible tracking deviations across both configurations. Third, fully coupled feedback revealed that rudimentary RPM-based power estimation underestimates energy requirements by 60% (1.87 vs. 1.17 kWh) due to transient aerodynamic shifts. Fourth, a clear engineering trade-off was identified: while the Dodecarotor achieved 1.4 times better per-passenger energy efficiency, its ride comfort was significantly compromised, identifying a critical barrier between efficiency and passenger experience. This pipeline provides a high-fidelity tool for quantitative vehicle selection during the conceptual design phase. Future work will investigate acceleration-clamping control to improve ride quality and evaluate performance under complex atmospheric disturbances and rotor-failure conditions.

Acknowledgments. This study was funded by the New Energy and Industrial Technology Development Organization (NEDO) under Grant No. JPNP14004.

References

1. Gomi, R., Takii, A., Yamakawa, M., Asao, S., Takeuchi, S., Nishimura, M.: Flight simulation from takeoff to yawing of eVTOL airplane with coaxial propellers by fluid-rigid body interaction. Advances in Aerodynamics **5**, 1–15 (2023). https://doi.org/10.1186/s42774-022-00133-x
2. Gong, A., Macneill, R., Verstraete, D.: Performance testing and modeling of a brushless DC motor, electronic speed controller and propeller for a small UAV application. In: 2018 AIAA Joint Propulsion Conference (2018). https://doi.org/10.2514/6.2018-4584, paper AIAA-2018-4584
3. Hagag, N., Hoeveler, B.: The feasibility of electric air taxis: Balancing time-savings and CO_2 emissions — A joint case study of respective plans in Paris. CEAS Aeronautical Journal **16**, 763–788 (2025). https://doi.org/10.1007/s13272-025-00811-8
4. Harten, A.: High resolution schemes for hyperbolic conservation laws. Journal of Computational Physics **135**(2), 260–278 (1997). https://doi.org/10.1016/0021-9991(83)90136-5
5. Hishida, M., Hashimoto, A., Murakami, K., Aoyama, T., Yamamoto, K.: A new slope limiter for fast unstructured CFD solver FaSTAR. In: Proceedings of 42nd Fluid Dynamics Conference/Aerospace Numerical Simulation Symposium. pp. 85–90. JAXA-SP-10-012 (2010), japan Aerospace Exploration Agency (in Japanese)
6. Kirste, A., Stumpf, E.: Development of a generalized eVTOL vehicle cost model for Urban Air Mobility operations. Journal of the Air Transport Research Society **5**, 100082 (2025). https://doi.org/10.1016/j.jatrs.2025.100082
7. Lee, S.M., Sa, J.H., Jeon, S.E., Kim, C.J., Park, S.H., Chung, K.H.: Aerodynamic design optimization of rotor airfoil with multiple constraints. Journal of Computational Fluid Engineering **15**(2), 79–85 (2010)

ICCS Camera Ready Version 2026
To cite this paper please use the final published version:
DOI: 10.1007/978-3-032-29921-5_22

8. Magata, T., Takii, A., Yamakawa, M., Takeuchi, S., Chung, Y.M.: Forward and turning flight simulation of flying cars and comparative evaluation of flight dynamics models considering wind disturbances. Journal of Computational Science **85**, 102519 (2025)
9. Roe, P.L.: Approximate Riemann solvers, parameter vectors, and difference schemes. Journal of Computational Physics **43**(2), 357–372 (1981). https://doi.org/10.1016/0021-9991(81)90128-5
10. Sato, H., Takii, A., Yamakawa, M., Kobayashi, Y., Asao, S., Takeuchi, S., Ikeda, T.: Comparison of crash simulations on two types of flying cars. In: International Conference on Computational Science (ICCS) (2025). https://doi.org/10.1007/978-3-031-97635-3_4
11. Schweiger, K., Preis, L.: Urban air mobility: Systematic review of scientific publications and regulations for vertiport design and operations. Aerospace **6**(7), 179 (2024). https://doi.org/10.3390/aerospace6070179
12. Takii, A., Gomi, R., Yamakawa, M., Tsubokura, M.: Turning flight simulation with fluid-rigid body interaction for flying car with contra-rotating propellers. In: International Conference on Computational Science (ICCS). pp. 566–577 (2023). https://doi.org/10.1007/978-3-031-35995-8_40
13. Takii, A., Yamakawa, M., Asao, S., Tajiri, K.: Six degrees of freedom numerical simulation of tilt-rotor plane. In: Lecture Notes in Computer Science. vol. 11536, pp. 506–519 (2019). https://doi.org/10.1007/978-3-030-22734-0_37
14. Takii, A., Yamakawa, M., Asao, S., Tajiri, K.: Six degrees of freedom flight simulation of tilt-rotor aircraft with nacelle conversion. Journal of Computational Science **44**, 101164 (2020)
15. Wambecq, A.: Rational Runge-Kutta methods for solving systems of ordinary differential equations. Computing **20**(4), 333–342 (1978). https://doi.org/10.1007/BF02252381
16. Wang, Y., Ji, H., Lu, L., Zhou, P.: Modeling multirotor wake interference in quadrotor eVTOL flight dynamics and handling qualities. Aerospace Science and Technology **165**, 110533 (2025). https://doi.org/10.1016/j.ast.2025.110533
17. Watanabe, K., Matsuno, K.: Moving computational domain method and its application to flow around a high-speed car passing through a hairpin curve. Journal of Computational Science and Technology **3**(2), 449–459 (2019)
18. Watanabe, S., Takahashi, T., Nagai, K.: Experimental study for aerodynamic performance of quadrotor helicopter. Transactions of the Japan Society for Aeronautical and Space Sciences **61**(1), 1–9 (2018)
19. Yamada, T., Semba, K., Sano, H., Suzuki, Y.: Simulation based design, a necessity for advanced design and requirement for CAE tools. IEEJ Journal of Industry Applications **12**(1), 1–11 (2023). https://doi.org/10.1541/ieejjia.22005984
20. Yamakawa, M., Takekawa, D., Matsuno, K., Asao, S.: Numerical simulation for a flow around body ejection using an axisymmetric unstructured moving grid method. Computational Thermal Sciences: An International Journal **4**(3) (2012)
21. Yeo, H.S.: Design and aeromechanics investigation of compound helicopters. Aerospace Science and Technology **88**, 158–173 (2019). https://doi.org/10.1016/j.ast.2019.03.010
22. Zhu, G., Jie, H., Zheng, Z., Hong, W.: MPC-based lateral motion control for autonomous vehicles through serially cascaded discretization method considering path preview. International Journal of Control, Automation, and Systems **22**(5), 1666–1679 (2024). https://doi.org/10.1007/s12555-023-0008-4

ICCS Camera Ready Version 2026
To cite this paper please use the final published version:
DOI: 10.1007/978-3-032-29921-5_22